coatings

MDPI

Article

Preparation and Self-Cleaning Properties of a Superhydrophobic Composite Coating on a Stainless Steel Substrate

Fengqin Li, Yuxue Hu, Xiaoming Feng * and Guizhong Tian *

School of Mechanical Engineering, Jiangsu University of Science and Technology, Zhenjiang 212000, China; lifengqin2021@just.edu.cn (F.L.); 221210201102@stu.just.edu.cn (Y.H.)
* Correspondence: xmfeng@just.edu.cn (X.F.); justtgz@163.com (G.T.)

Abstract: In order to improve the anti-fouling of stainless steel surfaces in outdoor or humid environments, a superhydrophobic modification is often used to improve its self-cleaning performance. However, the mechanical stability of superhydrophobic surfaces remains a challenge. In this paper, a two-step preparation method was adopted to prepare the micro–nanocomposite coating, which innovatively combined "top-down" and "bottom-up" approaches, and also coupled together two key factors that affect superhydrophobicity: a rough microstructure, and low surface energy. The silver mirror, adhesion, and pollution-resistance results show that the composite coating samples, which were obtained by optimizing the preparation process, have excellent water repellency and self-cleaning properties. Meanwhile, the samples demonstrate outstanding mechanical stability, and can resist damage from sandpaper and tape. The two-step preparation method was simple, fast, and efficient. This method could be popularized and applied to the preparation of superhydrophobic surfaces on metal substrates.

Keywords: superhydrophobic surface; micro–nanocomposite structure; self-cleaning; wear resistance

check for updates

Citation: Li, F.; Hu, Y.; Feng, X.; Tian, G. Preparation and Self-Cleaning Properties of a Superhydrophobic Composite Coating on a Stainless Steel Substrate. *Coatings* **2024**, *14*, 198. https://doi.org/10.3390/coatings14020198

Academic Editor: Joachim Albrecht

Received: 15 January 2024
Revised: 27 January 2024
Accepted: 31 January 2024
Published: 2 February 2024

1. Introduction

Due to the presence of the metal element molybdenum (Mo) in 316L stainless steel, it can withstand harsh working conditions [1], showing excellent corrosion resistance and weather resistance [2–5]. Therefore, this material is widely used in various engineering fields, such as harbor facilities [6,7], biomedical devices [8,9], and marine vessels [10,11]. However, when it is applied in a humid environment such as the ocean, the performance and service life of the material decreases [12–15]. Currently, in addition to adding chemical components to the substrate metal to improve its stability, improving the water resistance of the substrate surface, when combined with coating technology, has been a hot topic in the research field [16–19]. Some studies have reported that superhydrophobic surfaces can greatly improve the overall performance of the surface, such as corrosion resistance, stain resistance, and self-cleaning [20–24]. The most famous functional phenomenon of superhydrophobic surfaces is the self-cleaning effect of "lotus leaves". Water droplets can easily roll off the lotus leaf, carrying away contaminants from its surface and achieving self-cleaning [25]. It was also revealed that the lotus leaf effect is caused by the synergistic effect of the hierarchical rough structure and the low surface energy waxy material on its surface [26]. These are two core influences of superhydrophobic functional surfaces: a rough surface structure and low surface energy material [27–30]. With the development of technology, the low-cost, high-precision femtosecond–nanosecond laser has been widely used in texture engraving to obtain rough structures [31,32]. In regard to laser preparation technology, Khan et al. [33] investigated the role of pulse duration, scanning speed, and the surrounding environment of laser treatment on the wettability and self-cleaning properties of laser-structured aluminum, copper and galvanized steel plates using femtosecond fiber laser. Murillo et al. [34] studied the wettability behavior of hierarchical, multi-scale, periodic

surface patterns on the Ti-6Al-4V alloy by combining two laser micromachining techniques. In addition to the preparation process, the researchers carried out various functional studies based on the microstructure of the rough surface. Zhai et al. [35] investigated the bonding strength of a Zirconia coating and SUS304 stainless steel surface with different texture shapes and coverage using a nanosecond pulse laser. Volpe et al. [36] analyzed the superhydrophobicity and laser processing efficiency of three textured geometries, such as a square, triangle, and circle, on an aluminum alloy's surface. Khaskhoussi et al. [37] investigated the hydrophobicity and oleophilic behavior of different textured lead/lead-free bronze coatings. The research results showed that due to its good lipophilic properties, the porous structure's surface can be used as an oil reservoir to reduce the friction coefficient and improve lubrication performance. Dong et al. [38] prepared nano-rippled structures on a copper mesh using a femtosecond laser, demonstrating the dual characteristics of superhydrophobicity and superoleophilicity, along with a self-cleaning ability similar to that of a lotus leaf. In addition to the substrate texture, coupling low surface energy substances can also significantly improve the hydrophobicity or wear resistance of metal surfaces. Liu et al. [39] produced various surface micro-textures on 316L using a picosecond laser and deposited the chemical composition Al-5Si to analyze the wetting and spreading processes. Conradi et al. [40] coated FAS-SiO_2 nanoparticles with a superhydrophilic laser-textured AISI 316L surface to convert it into a (super)hydrophobic surface. At the same time, the surface roughness was changed by the direct laser machining of different separated microchannels so as to compare its influence on surface wettability. Xue et al. [41] constructed a novel Co-Ni/CeO_2 composite coating on carbon steel, exhibiting a high contact angle, an ultra-low sliding angle, and a self-cleaning effect.

This paper coupled together two key factors affecting superhydrophobicity, which are a rough microstructure and low surface energy, to prepare a micro–nanocomposite coating on the 316L substrate. A two-step preparation method was adopted, which innovatively combined "top-down" and "bottom-up" approaches to improve the stability of the functional coating. Firstly, the laser processing parameters of the substrate's microstructure were preliminarily optimized. Then, cinnamic acid, which is environmentally friendly, fluorine-free, and has low surface energy, was coated onto the microstructure to modify and enhance the superhydrophobicity. The superhydrophobic micro–nanocomposite coating prepared in this study was simple and had excellent self-cleaning performance and stability, which can be widely used in the industry and daily life.

2. Materials and Methods

2.1. Materials

This study employed 316L stainless steel as the substrate material, with the dimensions of 2 cm × 2 cm × 2 mm. The material was purchased from Wuxi Qingze Stainless Steel Co., Ltd. (Wuxi, China). The stainless steel substrate was prepared by sanding and ultrasonic cleaning with anhydrous ethanol before fabrication, aiming to remove impurities from the surface of the stainless steel substrate. The modifying material, myristoleic acid (CAS: 544-64-9), was purchased from Shanghai Aladdin Biochemical Technology Co., Ltd. (Shanghai, China).

2.2. Fabrication of Composite Coating

The superhydrophobic self-cleaning coating in this study was mainly prepared through a two-step process of laser engraving and material modification. The schematic diagram of the preparation process is shown in Figure 1.

First, a nanosecond laser micromachining system was used to carve the pre-treated stainless steel substrate and construct the required microstructure. After the engraving was completed, ultrasonic cleaning was performed to remove the metal debris remaining on the surface of the microstructure. Next, the superhydrophilic stainless steel substrate was immersed in a solution containing 0.1 mol/L of myristoleic acid and ethanol for two hours. During this process, the solution temperature was maintained at a constant 60 °C,

and a magnetic stirrer was used to ensure the uniform mixing of the solution. Then, the modified micro–nano substrate was ultrasonically cleaned to remove excess myristoleic acid from the surface. Finally, the samples were placed in a 60 °C oven for 1 h to complete the preparation. During the microstructure engraving process, the preparation parameters significantly affected the morphology. To obtain a better superhydrophobic self-cleaning surface, the engraving process was optimized.

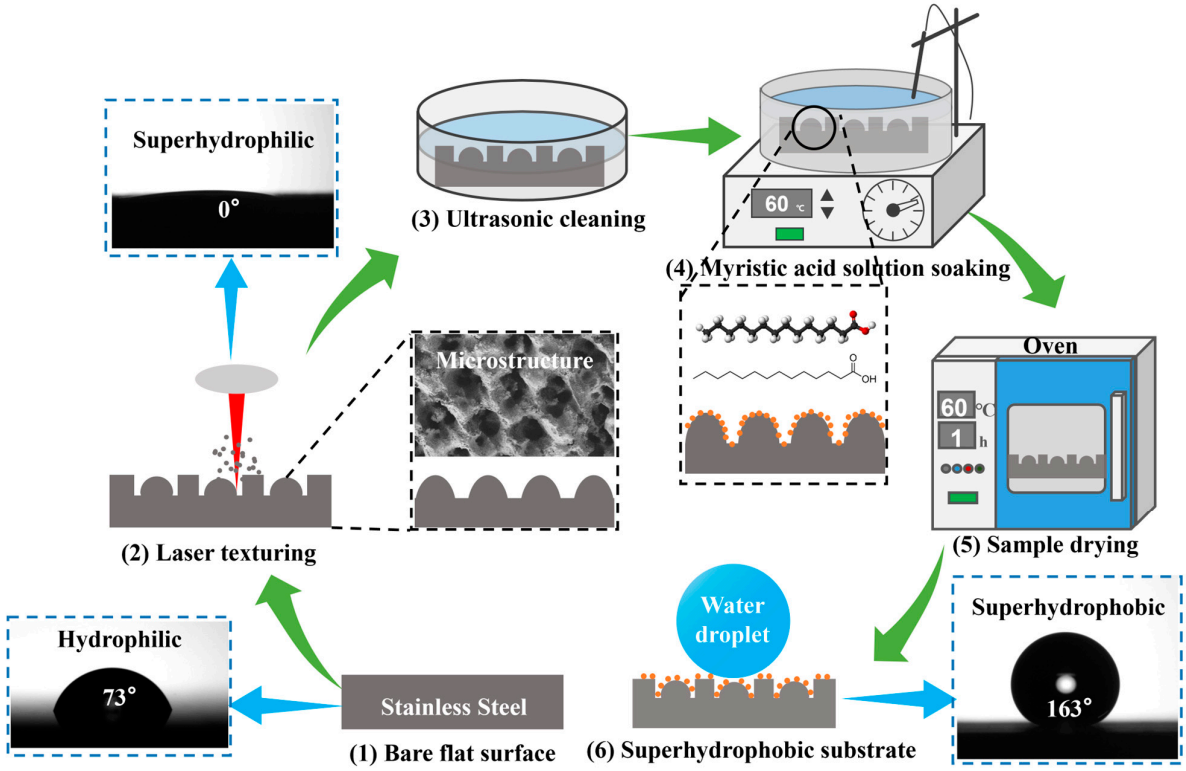

Figure 1. Preparation process of laser/myristic acid superhydrophobic surface.

2.3. Characterization

This article employed a laser confocal morphological microscope (VK-X1000, Keyence, Osaka, Japan) to characterize the surface microstructure of the samples and analyze roughness. The laser had a wavelength of 408 nm, a maximum output power of 0.9 MW, and a display resolution of 0.5 nm. The contact angle values on the sample surface were determined using an optical contact angle meter (Theta Lite, Biolin Scientific, Gothenburg, Sweden) with a water droplet volume of 5 µL. The dynamic behaviors of the liquid were recorded using a high-speed camera (PCO dimax S1, Munich, Germany). Before the test, the observation position was aligned, and the focus was adjusted. Subsequently, the detailed process of the droplet viscosity or rolling down the surface was captured in real time. After testing, the instantaneous images were processed and analyzed using DW Ruler software (One Attension v2.2).

2.4. Performance Test

2.4.1. Superhydrophobicity Test

The superhydrophobic properties of the samples were tested through both macroscopic and microscopic observations. During macroscopic characterization, a tweezer was used to hold a corner of the sample, and then the sample was immersed in a beaker filled with water and slowly removed. The status of the sample throughout the immersion/extraction process was recorded. During the microscopic characterization, a contact angle measurement instrument was combined with a high-speed camera to record the adhesion characteristics of a 5 µL droplet when it came into contact with the sample.

2.4.2. Self-Cleaning Performance Test

During this stage, a high-speed camera was used to record the anti-fouling self-cleaning process of the sample from two perspectives: the side view and the top view. The samples were placed on the platform at a certain inclined angle, and quartz sand was used as the contaminant, which was uniformly sprinkled on the surface. There was a syringe on top of the sample to control the release of water droplets. Water droplets from the syringe were squeezed out and fell on the surface of the sample. A high-speed camera was used to capture the movement of the falling droplets onto the sample surface, allowing for a comparative analysis of self-cleaning properties.

2.4.3. Stability Test of the Sample Coating

The stability of the sample coating was studied using the tape peeling test and sandpaper wear test, and the water contact angle was used to assess the degree of performance degradation. During the tape peeling experiment, the tape was adhered to the surface of the sample, and gentle pressure was applied to ensure uniform contact between the tape and the sample surface. Then, the tape was slowly peeled off. The test was repeated 12 times. Sandpaper wear is the most commonly used method to evaluate the mechanical robustness of coatings. In this study, the ISO standard 8251-2018 for sandpaper wear testing was employed [42]. The sample was affixed to the bottom of a 100 g weight using double-sided tape, with the coated side facing 1500-grit sandpaper. The sample was then pushed uniformly for 20 cm (one cycle). The wear cycle was set to 40 times. During the wear test, the hydrophobic surface of the sample was brought into contact with the sandpaper, with a 100 g weight placed on the back. The sample was then pushed uniformly for 20 cm (one cycle). The number of cycles was set to 40.

3. Results and Discussion

3.1. Optimization of Microstructure Preparation Process

As for the microstructure's morphology on the surface, the convex hull structure of the array arrangement was chosen. The schematic diagram for the design is shown in Figure 2a. The microstructure's size was about 20 μm. The surface microstructure was prepared using a laser micromachining system, as shown in Figure 2b. The rated power of the laser in this system was 5 watts, and the thermal-affected zone which it generated was at the micrometer level. Its minimum spot size was around 5 μm, allowing for the engraving of micrometer-scale features.

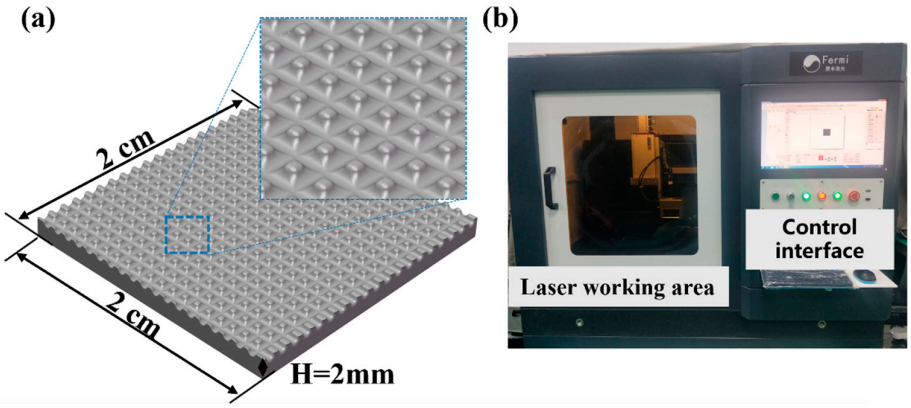

Figure 2. (**a**) Surface microstructure design; (**b**) laser micromachining system.

The main processing parameters that affect the surface microstructure include the number of scanning cycles (t), the frequency (f), and the pulse width (w). Among them, the number of scanning cycles affects the depth of the microstructure, while the frequency and pulse width affect the morphology of the microstructure. This section analyzes them separately.

3.1.1. Optimization of the Number of Scanning Cycles

This study first evaluated the influence of the laser scanning cycle (t) on the 316L substrate. The scanning cycle was set to 5, 10, 15, and 20 times, and the resulting surface roughness is shown in Figure 3a.

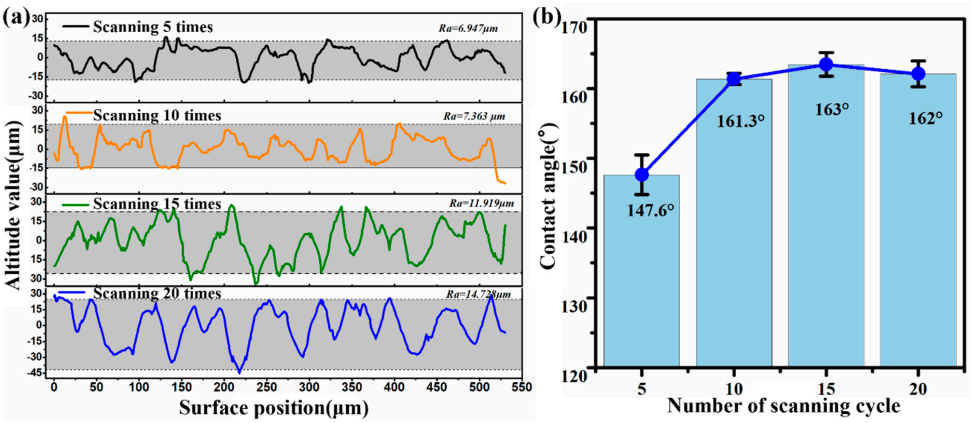

Figure 3. The influence of the number of scanning cycles on the surface: (**a**) the degree of roughness; (**b**) the water contact angle.

It can be observed that with the increase in the number of laser-marking cycles, the surface height values fluctuate more widely. The corresponding Ra values measured are 6.95, 7.36, 11.92, and 14.73. This indicates that the substrate surface becomes increasingly rough, providing conditions for the formation of a superhydrophobic surface.

To further investigate the influence of the scanning times on subsequent low surface energy modification, the samples were modified with myristoleic acid under the same modification parameters. The water contact angles measured on the samples are shown in Figure 3b. It can be observed that when scanned five times, the contact angle was 147.6 ± 2.85°, which did not reach superhydrophobicity. After scanning 10 times or more, the contact angle values tended to stabilize and remain above 160°. The specific contact angle values were 161.3 ± 0.81°, 163.45 ± 1.70°, and 162.1 ± 1.84°, respectively, with only slight fluctuations. The samples exhibited a superhydrophobic state. Considering the impact of laser energy and metal spatter, too many scanning cycles may have a negative effect on the stability of the engraving morphology. Therefore, 10 scanning cycles were chosen as the scanning parameter for the subsequent samples.

3.1.2. Optimization of Laser Parameters

To achieve the morphology designed, an analysis of the frequency (f) and pulse width (w) was conducted with the scanning cycles determined. Since the equipment specifies that the product of frequency and pulse width should not exceed 1000 (the duty cycle should not exceed 100%), the specific process parameters were set as shown in Table 1.

Table 1. Laser processing parameters, corresponding surface roughness, and contact angle.

Sample	Name	Frequency f (kHz)	Pulse Width w (μs)	f*w	Modification (0.1 mol/mL)	Ra (μm)	WAC (°)
Stainless steel bare substrate	SS	0	0	0	no	/	73 ± 4.38°
Substrate and modification	SSM	0	0	0	yes	0.853	106.5 ± 2.76°
Laser engraving and modification	LM-200	40	5	200		2.638	156 ± 1.49°
	LM-400	80	5	400		4.178	158.8 ± 1.13°
	LM-600	100	6	600		4.629	158.1 ± 2.77°
	LM-800	80	10	800		7.363	163 ± 1.76°
	LM-1000	100	10	1000		16.458	158.9 ± 1.75°

The morphology after laser engraving was captured using a laser confocal measuring microscope (VK-X1000). The results are shown in Figure 4.

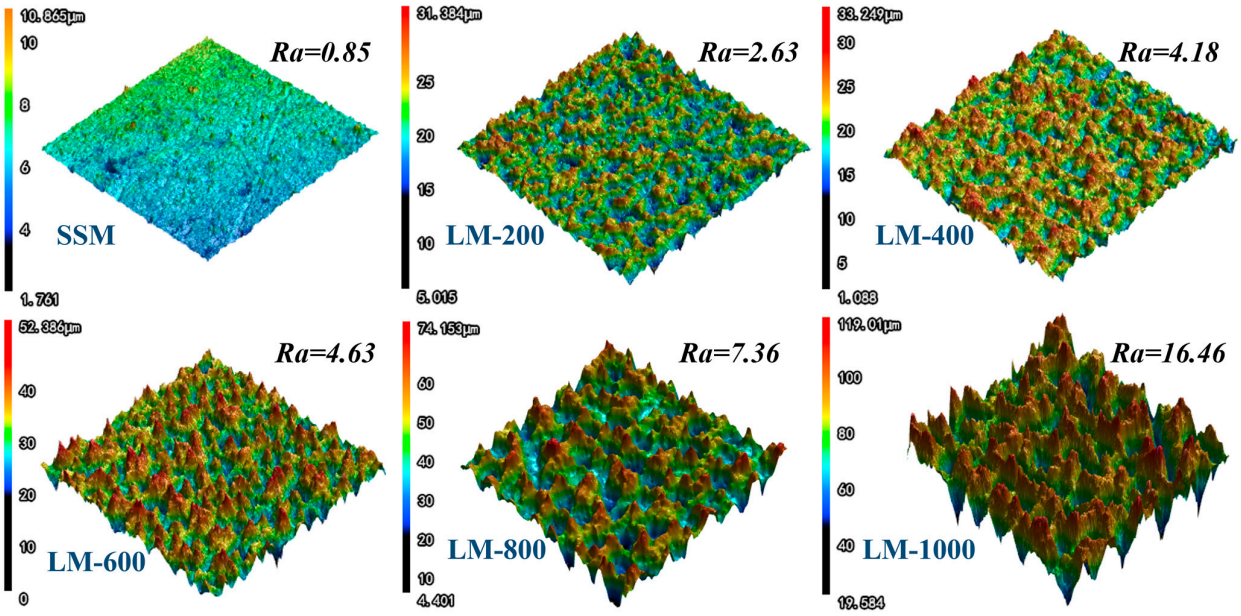

Figure 4. Surface micro-topography and surface roughness of each sample.

It can be observed that the surface of the stainless steel substrate, after laser ablation, exhibited dense pits and protrusions in the scanned area. With the increase in the frequency times pulse width, the morphology of the pits and protrusions became more pronounced, forming a peak–valley microstructure on the surface. The specific roughness values are shown in the right column of Table 1. The roughness of sample LM-800 was 7.36, and the roughness of sample LM-1000 was 16.46. To explore the ideal laser parameters, the stainless steel samples with constructed microstructures were subjected to modification with a 0.1 mol/L myristoleic acid/ethanol solution. The contact angles and surface morphologies of the samples are shown in Figure 5.

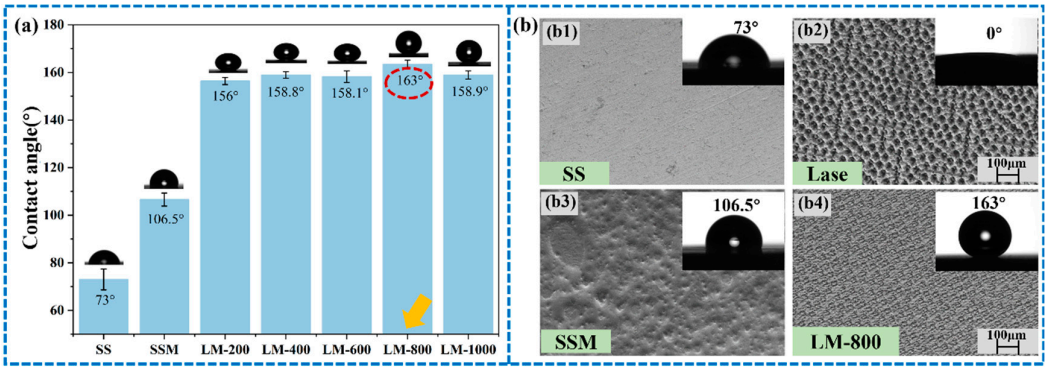

Figure 5. (**a**) Surface contact angle of samples; (**b**) comparison of surface morphology with or without myristate modification.

From Figure 5a, it can be observed that the contact angle of the bare 316 stainless steel substrate sample (SS) is 73 ± 4.38°, exhibiting hydrophilicity. After low surface energy modification, the contact angle of the sample (SSM) increased to 106.5 ± 2.76°. However, after laser treatment and modification, the samples (LM200~LM1000) exhibited a surface contact angle greater than 150°, demonstrating superhydrophobicity. Among them, when the laser frequency was 80 kHz, the Q pulse width was 10 μs, and the surface contact angle

of the sample reached a peak of 163 ± 1.76°. The wettability of sample surfaces can be explained using the Wenzel and Cassie–Baxter theoretical models. According to the Wenzel wetting model [43], Equation (1) is as follows:

$$\cos\theta_m = r\cos\theta_\gamma \quad (1)$$

where θ_m is the apparent contact angle; θ_γ is Young's contact angle; and r represents the surface roughness factor.

The value of r is always greater than one. As a result, an increase in surface roughness directly amplifies the solid surface's wettability, in which the lyophilic and lyophobic surfaces become more lyophobic and lyophilic. Therefore, after the microstructure was carved on the hydrophilic stainless steel surface (73 ± 4.38°), the substrate surface became rougher, and the contact angle also decreased sharply, showing a super hydrophilic contact angle (0°).

Superhydrophobicity can be explained using the Cassie–Baxter theory model [44], which is represented by the following Equation (2):

$$\cos\theta_{cb} = f_1\cos\theta_1 + f_2\cos\theta_2 = f_1(\cos\theta_1 + 1) - 1 \quad (2)$$

where θ_1 and θ_2 are the intrinsic contact angles of water droplets on solids and gases, and here, $\theta_2 = 180°$; f_1 and f_2 are the fraction of the apparent contact area between the solid–liquid contact area and the gas–liquid contact area ($f_1 + f_2 = 1$).

Equation (2) describes the contact state between the water droplets and the substrate surface in the liquid–gas–solid three-phase composite state. The morphology images in Figure 5(b4) demonstrate the uniformity of the sample. While the frequency continued to increase, Figure 5a shows a decrease in the contact angle of the sample (LM-1000). The analysis suggests that when the laser energy is excessively increased, the etching reaction becomes excessively intense, leading to a large amount of splashing, solidification, and the accumulation of metal splatters on the surface of the sample. This results in a reduction in the formed surface area. Therefore, based on the contact angle and morphological results of the samples, the optimized laser parameters were determined to have a frequency of 80 kHz and a Q pulse width of 10 μs.

3.2. Superhydrophobicity Testing of Samples

According to the optimized processing parameters mentioned above, the surface microstructure was engraved, and the low surface energy material, myristoleic acid, was used for the modification. The preparation of superhydrophobic composite coating samples was completed, followed by the testing and analysis of their superhydrophobicity. Figure 6 illustrates the entire process of immersing and removing the sample. From Figure 6(a3), it can be observed that the surface of the immersed sample exhibited a silver mirror effect. This was caused by the rough structure on the surface of the superhydrophobic stainless steel sample, which trapped air and resulted in the reflection of light near its surface [16].

Afterward, the hydrophobicity of the sample was analyzed using a high-speed camera combined with the contact angle meter. The testing process is illustrated in Figure 7.

From Figure 7(a2,a3), it can be observed that when the sample came into contact with the water droplet, the water droplet underwent deformation due to the compression on the sample surface. As the sample slowly descended with the loading stage, the bottom of the water droplet was elongated (Figure 7(a4,a5)), and the droplet detached from the surface of the sample without adhesion occurring.

The macroscopic and microscopic test results indicate that the composite-coated sample exhibited excellent superhydrophobic performance.

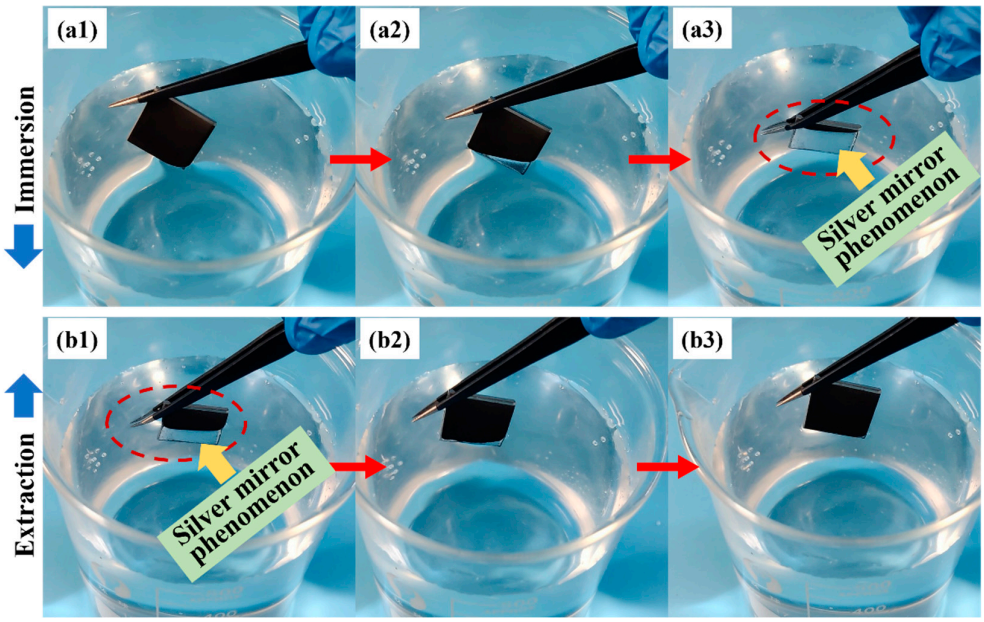

Figure 6. Silver mirror phenomenon during immersion (**a1**–**a3**) and extraction (**b1**–**b3**) of superhydrophobic LM-800 sample.

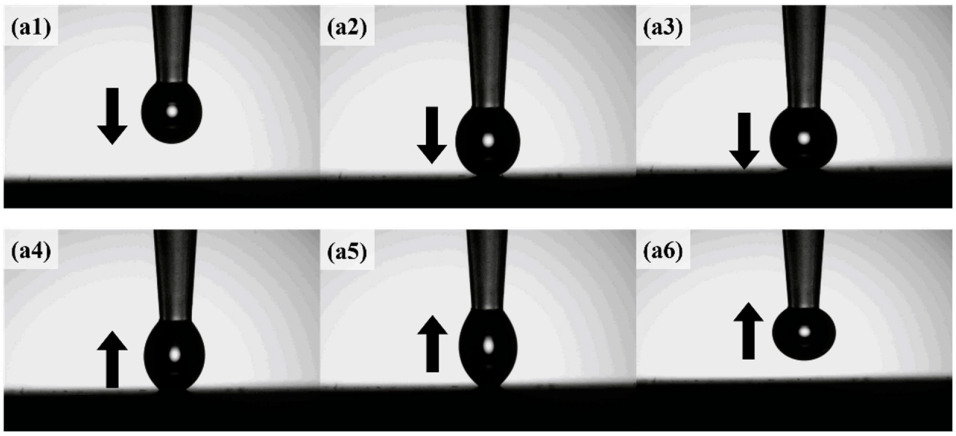

Figure 7. Adhesion test of the sample. Subfigure a1–a6 shows the entire process of the droplet approaching, touching and leaving the sample surface, and arrows show the direction of the droplet moving.

3.3. Self-Cleaning Performance Test

We continued to conduct tests and analyses on the self-cleaning performance of the composite-coated samples. The test results from the two perspectives are shown in Figures 8 and 9.

The results in Figure 8(a1–a4) show that there was a significant resistance between the water droplet and the surface of the stainless steel bare substrate. The water droplet almost adhered to the surface. The water droplet was unable to carry away the quartz sand particles, and the sample did not achieve self-cleaning. For the superhydrophobic sample, as shown in Figure 8(b1–b4), the water droplet fell onto the surface, condensing into a spherical shape (Figure 8(b2)), and then rolled off the sample (Figure 8(b3)). During this process, the water droplet carried away the quartz sand pollutants, leaving behind a clean trail (Figure 8(b4)), and the sample achieved self-cleaning.

Figure 9 shows the entire self-cleaning process of dynamic water droplets removing quartz sand pollutants from the sample, which is captured from an overhead angle with a high-speed camera.

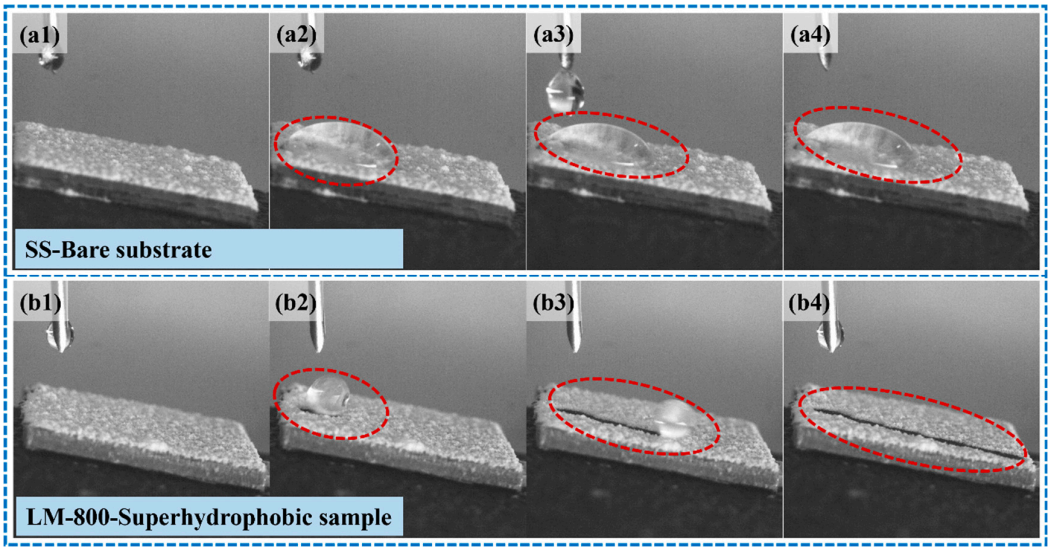

Figure 8. Self-cleaning test from a side shot view: (**a1**–**a4**) bare stainless steel substrate sample; (**b1**–**b4**) superhydrophobic sample.

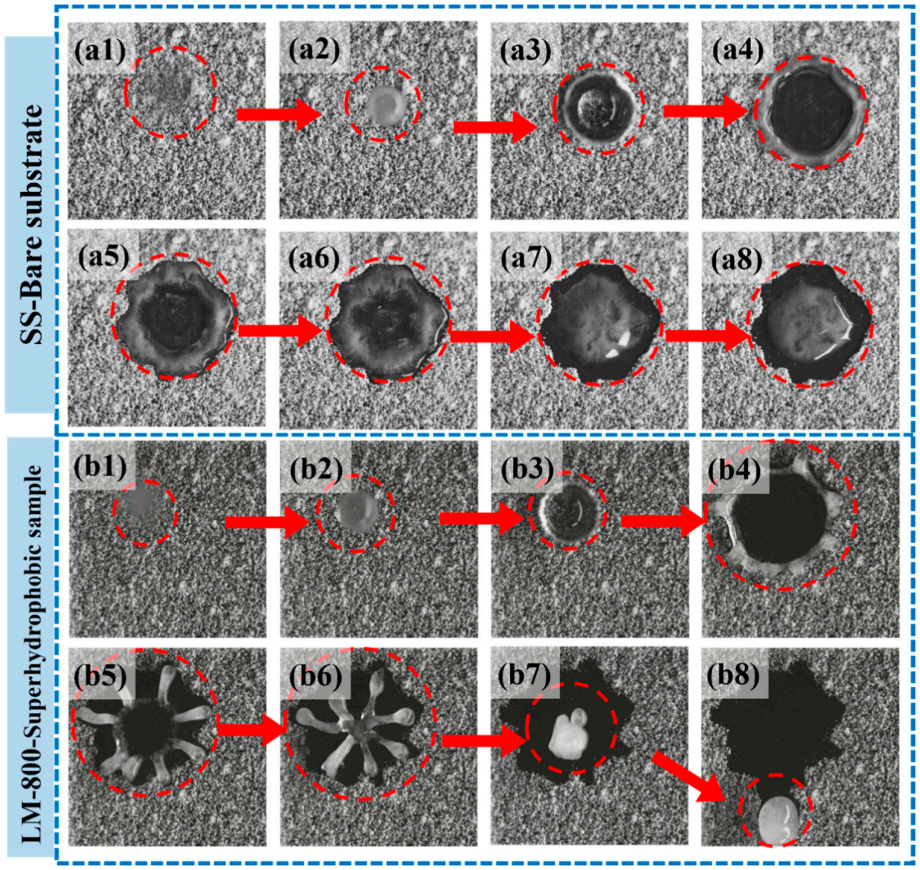

Figure 9. Self-cleaning test from an overhead view: (**a1**–**a8**) bare stainless steel substrate sample; (**b1**–**b8**) superhydrophobic sample.

In Figure 9(a1–a4), it can be observed that when the water droplet impacted the surface of the bare substrate (SS), the quartz sand in the impacted area spread outward in a circular pattern as the droplet expanded. As the water droplet retracted (Figure 9(a5–a8)), quartz sand gradually converged toward the center. Due to the hydrophilic characteristics of the surface, significant viscous forces acted on the water droplet, preventing it from bouncing off the surface. At this point, the water droplet, mixed with the surrounding quartz

sand, adhered to the bare substrate surface, and the surface did not exhibit self-cleaning properties.

However, when the water droplet impacted the surface of the superhydrophobic sample (LM-800), the dynamic process was completely different. As the water droplet spread out in a pearl necklace-like pattern upon compression, it started to contract toward the center, evolving into a petal shape while carrying quartz sand particles (Figure 9(b5,b6)), and then gathering into a spherical form (Figure 9(b7)). Finally, the quartz sand, along with the bouncing water droplet, left the sample. The area in contact with the water droplet showed a clean effect (Figure 9(b8)). It can be observed that the prepared superhydrophobic sample had excellent self-cleaning performance.

3.4. Stability Test of the Composite Coating

In practical industrial applications, stainless steel materials are commonly used outdoors, and their service environment is often challenging. The stability of surface coatings significantly affects their performance. Therefore, this study evaluates the stability of the prepared superhydrophobic composite coating samples through tape peeling and sandpaper abrasion tests to assess their superhydrophobic performance.

The test results are shown in Figure 10. The contact angle of the sample slightly decreased, but the values remained above 150°, indicating that the superhydrophobicity was still maintained. The reason for the slight decrease in the contact angle may be attributed to the fact that the surface-engineered microstructures provided more physical attachment points for myristoleic acid, resulting in higher binding strength. As a result, it was less prone to removal during the peeling and tearing action of the tape. Additionally, the chemical branches of COOH groups in myristoleic acid form stable complexes on the surface, providing stability and resistance against the peeling action of the tape.

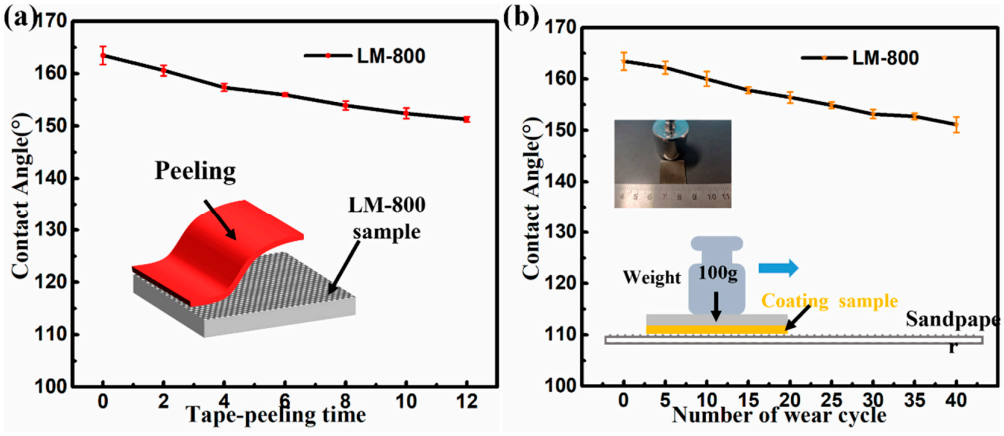

Figure 10. Stability test of sample: (**a**) tape stripping test; (**b**) sandpaper wear test.

For wear testing, the sample underwent 40 cycles. The change in the contact angle of the sample is shown in Figure 10b. It can be observed that after 40 cycles of wear testing, the contact angle of the sample was 151.1°, indicating superhydrophobicity. Although high-intensity wear cycles caused a decrease in the water contact angle of the samples, they still maintained good hydrophobicity. The combined results of peeling and wear indicate that the composite coating, coupling a microstructure with kaempferol, exhibits excellent stability.

4. Conclusions

This article first utilized a "top-down" approach with nanosecond laser technology to construct a peak–valley microstructure on the surface of 316L. Subsequently, it combined a "bottom-up" approach involving the deposition of myristoleic acid to modify the microstructure, completing the two-step process for the construction and preparation of a

superhydrophobic surface. Based on the experimental results, the following conclusions are obtained: (1) The contact angle of the composite coating sample can reach 163°, indicating low adhesion and excellent superhydrophobicity. (2) The composite coating sample resisted the attachment of pollutants, exhibiting self-cleaning properties. (3) The composite coating demonstrated resistance to peeling and wear, displaying good stability. 4) The preparation method used in this study was simple, efficient, and rapid, making it suitable for the widespread application of preparing superhydrophobic surfaces on metal substrates.

Author Contributions: Conceptualization, F.L. and X.F.; methodology, F.L. and Y.H.; writing—original draft preparation, F.L.; writing—review and editing, X.F. and G.T.; supervision, G.T. All authors have read and agreed to the published version of the manuscript.

Funding: This work was funded by the National Natural Science Foundation of China (No. 52305605 and 52375291), the Natural Science Foundation of the Jiangsu Higher Education Institutions of China (No. 22KJB430022), and the Science Research Project of Jiangsu University of Science and Technology (No. 1022932106).

Institutional Review Board Statement: Not applicable.

Informed Consent Statement: Not applicable.

Data Availability Statement: Data are contained within the article.

Conflicts of Interest: The authors declare no conflict of interest.

References

1. Duan, T.; Peng, W.; Ding, K.; Guo, W.; Hou, J.; Cheng, W.; Liu, S.; Xu, L. Long-term field exposure corrosion behavior investigation of 316L stainless steel in the deep sea environment. *Ocean Eng.* **2019**, *189*, 106405. [CrossRef]
2. Li, B.; Wang, T.; Li, P.; Wang, S.; Wang, A.L. Selective Laser Melting of 316L Stainless Steel: Influence of Co-Cr-Mo-W Addition on Corrosion Resistance. *Metals* **2021**, *11*, 597. [CrossRef]
3. Tsuge, S. Recent Advances in Stainless Steel. *Encycl. Mater. Met. Alloys* **2022**, *2*, 200–207. [CrossRef]
4. Lian, X.; Cui, H.; Wang, Q.; Song, X.; Yang, X.; Cui, Z. Corrosion and mechanical behavior of amorphous-nanocrystalline NiCrMo coatings. *J. Alloys Compd.* **2022**, *927*, 167010. [CrossRef]
5. Borgioli, F.; Galvanetto, E.; Bacci, T. Low temperature nitriding of AISI 300 and 200 series austenitic stainless steels. *Vacuum* **2016**, *127*, 51–60. [CrossRef]
6. Kaya, Y.; Kahraman, N. An investigation into the explosive welding/cladding of Grade A ship steel/AISI 316L austenitic stainless steel. *Mater. Des.* **2013**, *52*, 367–372. [CrossRef]
7. Lei, Y.B.; Wang, Z.B.; Zhang, B.; Luo, Z.P.; Lu, J.; Lu, K. Enhanced mechanical properties and corrosion resistance of 316L stainless steel by pre-forming a gradient nanostructured surface layer and annealing. *Acta Mater.* **2021**, *208*, 116773. [CrossRef]
8. Lodhi, M.J.K.; Deen, K.M.; Greenlee-Wacker, M.C.; Haider, W. Additively manufactured 316L stainless steel with improved corrosion resistance and biological response for biomedical applications. *Addit. Manuf.* **2019**, *27*, 8–19. [CrossRef]
9. Bruschi, S.; Pezzato, L.; Ghiotti, A.; Dabalà, M.; Bertolini, R. Effectiveness of using low-temperature coolants in machining to enhance durability of AISI 316L stainless steel for reusable biomedical devices. *J. Manuf. Process.* **2019**, *39*, 295–304. [CrossRef]
10. Sharma, S.K.; Singh, A.K.; Mishra, R.K.; Shukla, A.K.; Sharma, C. Processing Techniques, Microstructural and Mechanical Properties of Additive Manufactured 316L Stainless Steel: Review. *J. Inst. Eng. Ser. D* **2023**. [CrossRef]
11. Gupta, S.; Singh, D.; Yadav, A.; Jain, S.; Pratap, B. A comparative study of 5083 aluminium alloy and 316L stainless steel for shipbuilding material. *Mater. Today: Proc.* **2020**, *28*, 2358–2363. [CrossRef]
12. Liu, H.; He, J.; Jin, Z.; Liu, H. Pitting corrosion behavior and mechanism of 316L stainless steel induced by marine fungal extracellular polymeric substances. *Corros. Sci.* **2023**, *224*, 111485. [CrossRef]
13. Dong, P.; Scatigno, G.G.; Wenman, M.R. Effect of Salt Composition and Microstructure on Stress Corrosion Cracking of 316L Austenitic Stainless Steel for Dry Storage Canisters. *J. Nucl. Mater.* **2021**, *545*, 152572. [CrossRef]
14. Chandra, K.; Kain, V.; Kumar, N. Failure Cases of Stainless Steel 316/316L Pipe Welds in Moist Hydrogen Sulfide Environment. *J. Fail. Anal. Prev.* **2022**, *22*, 478–490. [CrossRef]
15. Morsiya, C. A review on parameters affecting properties of biomaterial SS 316L. *Aust. J. Mech. Eng.* **2022**, *20*, 803–813. [CrossRef]
16. Wang, F.; Pi, J.; Song, F.; Feng, R.; Xu, C.; Wang, X.-L.; Wang, Y.-Z. A superhydrophobic coating to create multi-functional materials with mechanical/chemical/physical robustness. *Chem. Eng. J.* **2020**, *381*, 122539. [CrossRef]
17. Zeng, Q.; Zhou, H.; Huang, J.; Guo, Z. Review on the recent development of durable superhydrophobic materials for practical applications. *Nanoscale* **2021**, *13*, 11734–11764. [CrossRef]
18. Hoque, M.J.; Ma, J.; Rabbi, K.F.; Yan, X.; Singh, B.P.; Upot, N.V.; Fu, W.; Kohler, J.; Thukral, T.S.; Dewanjee, S.; et al. Perspectives on superhydrophobic surface durability. *Appl. Phys. Lett.* **2023**, *123*, 110501. [CrossRef]

19. Zhan, Y.; Yu, S.; Amirfazli, A.; Siddiqui, A.R.; Li, W. Facile preparations of superhydrophobic coatings with self-cleaning, mechanical durability, anticorrosion and easy-repairable properties. *Mater. Res. Express* **2022**, *9*, 065302. [CrossRef]
20. Dalawai, S.P.; Saad Aly, M.A.; Latthe, S.S.; Xing, R.; Sutar, R.S.; Nagappan, S.; Ha, C.-S.; Kumar Sadasivuni, K.; Liu, S. Recent Advances in durability of superhydrophobic self-cleaning technology: A critical review. *Prog. Org. Coat.* **2020**, *138*, 105381. [CrossRef]
21. Hooda, A.; Goyat, M.S.; Pandey, J.K.; Kumar, A.; Gupta, R. A review on fundamentals, constraints and fabrication techniques of superhydrophobic coatings. *Prog. Org. Coat.* **2020**, *142*, 105557. [CrossRef]
22. Wu, Y.; Du, J.; Liu, G.; Ma, D.; Jia, F.; Klemeš, J.J.; Wang, J. A review of self-cleaning technology to reduce dust and ice accumulation in photovoltaic power generation using superhydrophobic coating. *Renew. Energy* **2022**, *185*, 1034–1061. [CrossRef]
23. Goharshenas Moghadam, S.; Parsimehr, H.; Ehsani, A. Multifunctional superhydrophobic surfaces. *Adv. Colloid. Interface Sci.* **2021**, *290*, 102397. [CrossRef] [PubMed]
24. Samaha, M.A.; Tafreshi, H.V.; Gad-el-Hak, M. Superhydrophobic surfaces: From the lotus leaf to the submarine. *Comptes Rendus Mécanique* **2012**, *340*, 18–34. [CrossRef]
25. Sun, S.; Li, H.; Guo, Y.; Mi, H.-Y.; He, P.; Zheng, G.; Liu, C.; Shen, C. Superefficient and robust polymer coating for bionic manufacturing of superwetting surfaces with "rose petal effect" and "lotus leaf effect". *Prog. Org. Coat.* **2021**, *151*, 106090. [CrossRef]
26. Borchers, A.; Pieler, T. Programming pluripotent precursor cells derived from Xenopus embryos to generate specific tissues and organs. *Genes* **2010**, *1*, 413–426. [CrossRef] [PubMed]
27. Bayer, I.S. Superhydrophobic Coatings from Ecofriendly Materials and Processes: A Review. *Adv. Mater. Interfaces* **2020**, *7*, 2000095. [CrossRef]
28. Wang, D.; Sun, Q.; Hokkanen, M.J.; Zhang, C.; Lin, F.-Y.; Liu, Q.; Zhu, S.-P.; Zhou, T.; Chang, Q.; He, B.; et al. Design of robust superhydrophobic surfaces. *Nature* **2020**, *582*, 55–59. [CrossRef]
29. Parvate, S.; Dixit, P.; Chattopadhyay, S. Superhydrophobic Surfaces: Insights from Theory and Experiment. *J. Phys. Chem. B* **2020**, *124*, 1323–1360. [CrossRef]
30. Bittoun, E.; Marmur, A. The Role of Multiscale Roughness in the Lotus Effect: Is It Essential for Super-Hydrophobicity? *Langmuir* **2012**, *28*, 13933–13942. [CrossRef]
31. Chen, Z.; Yang, J.; Liu, H.; Zhao, Y.; Pan, R. A short review on functionalized metallic surfaces by ultrafast laser micromachining. *Int. J. Adv. Manuf. Technol.* **2022**, *119*, 6919–6948. [CrossRef]
32. Safari, M.; Alves de Sousa, R.; Joudaki, J. Recent Advances in the Laser Forming Process: A Review. *Metals* **2020**, *10*, 1472. [CrossRef]
33. Khan, S.A.; Boltaev, G.S.; Iqbal, M.; Kim, V.; Ganeev, R.A.; Alnaser, A.S. Ultrafast fiber laser-induced fabrication of superhydrophobic and self-cleaning metal surfaces. *Appl. Surf. Sci.* **2021**, *542*, 148560. [CrossRef]
34. Huerta-Murillo, D.; Aguilar-Morales, A.I.; Alamri, S.; Cardoso, J.T.; Jagdheesh, R.; Lasagni, A.F.; Ocaña, J.L. Fabrication of multi-scale periodic surface structures on Ti-6Al-4V by direct laser writing and direct laser interference patterning for modified wettability applications. *Opt. Lasers Eng.* **2017**, *98*, 134–142. [CrossRef]
35. Zhai, Z.; Qu, Y.; Zhang, H.; Wang, B.; Zhang, Y.; Cui, Y. Fabrication of microtexture by pulse laser to improve the bonding strength of coating. *Optik* **2022**, *265*, 169556. [CrossRef]
36. Volpe, A.; Covella, S.; Gaudiuso, C.; Ancona, A. Improving the Laser Texture Strategy to Get Superhydrophobic Aluminum Alloy Surfaces. *Coatings* **2021**, *11*, 369. [CrossRef]
37. Khaskhoussi, A.; Risitano, G.; Calabrese, L.; D'Andrea, D. Investigation of the Wettability Properties of Different Textured Lead/Lead-Free Bronze Coatings. *Lubricants* **2022**, *10*, 82. [CrossRef]
38. Dong, Z.; Sun, X.; Kong, D.; Chu, D.; Hu, Y.; Duan, J.-A. Spatial light modulated femtosecond laser ablated durable superhydrophobic copper mesh for oil-water separation and self-cleaning. *Surf. Coat. Technol.* **2020**, *402*, 126254. [CrossRef]
39. Liu, Z.; Yang, J.; Li, Y.; Li, W.; Chen, J.; Shen, L.; Zhang, P.; Yu, Z. Wetting and spreading behaviors of Al-Si alloy on surface textured stainless steel by ultrafast laser. *Appl. Surf. Sci.* **2020**, *520*, 146316. [CrossRef]
40. Conradi, M.; Drnovsek, A.; Gregorcic, P. Wettability and friction control of a stainless steel surface by combining nanosecond laser texturing and adsorption of superhydrophobic nanosilica particles. *Sci. Rep.* **2018**, *8*, 7457. [CrossRef]
41. Xue, Y.; Wang, S.; Xue, Y.; Cao, L.; Nie, M.; Jin, Y. Robust Self-Cleaning and Marine Anticorrosion Super-Hydrophobic Co–Ni/CeO_2 Composite Coatings. *Adv. Eng. Mater.* **2020**, *22*, 2000402. [CrossRef]
42. *ISO 8251-2018*; Anodizing of Aluminium and Its Alloys—Measurement of Abrasion Resistance of Anodic Oxidation Coatings. ISO: Geneva, Switzerland, 2018. Available online: https://www.iso.org/standard/72812.html (accessed on 10 January 2024).
43. Wenzel, R.W. Resistance of Solid Surfaces to Wetting by Water. *Ind. Eng. Chem.* **1936**, *28*, 988–994. [CrossRef]
44. Cassie, A.B.D.; Baxter, S. Wettability of porous surfaces. *Trans. Faraday Soc.* **1944**, *40*, 546. [CrossRef]